NeuroImage 291 (2024) 120595

Contents lists available at ScienceDirect

NeuroImage

journal homepage: www.elsevier.com/locate/ynimg

GAN-MAT: Generative adversarial network-based microstructural profile covariance analysis toolbox

Yeongjun Park [a], Mi Ji Lee [b], Seulki Yoo [c], Chae Yeon Kim [d], Jong Young Namgung [d], Yunseo Park [d], Hyunjin Park [e,f], Eun-Chong Lee [g], Yeo Dong Yoon [g], Casey Paquola [h], Boris C. Bernhardt [i], Bo-yong Park [d,f,j,*]

[a] *Department of Electrical and Computer Engineering, Sungkyunkwan University, Suwon, South Korea*
[b] *Department of Neurology, Seoul National University Hospital, Seoul National University College of Medicine, Seoul, South Korea*
[c] *GE HealthCare Korea, Seoul, South Korea*
[d] *Department of Data Science, Inha University, Incheon, South Korea*
[e] *School of Electronic and Electrical Engineering, Sungkyunkwan University, Suwon, South Korea*
[f] *Center for Neuroscience Imaging Research, Institute for Basic Science, Suwon, South Korea*
[g] *Poderosa, Seoul, South Korea*
[h] *Institute of Neuroscience and Medicine (INM-1), Forschungszentrum Jülich, Jülich, Germany*
[i] *McConnell Brain Imaging Centre, Montreal Neurological Institute and Hospital, McGill University, Montreal, Quebec, Canada*
[j] *Department of Statistics and Data Science, Inha University, Incheon, South Korea*

ARTICLE INFO

Keywords:
Structural magnetic resonance imaging
Generative adversarial network
Microstructure-sensitive proxy
Microstructural gradient

ABSTRACT

Multimodal magnetic resonance imaging (MRI) provides complementary information for investigating brain structure and function; for example, an *in vivo* microstructure-sensitive proxy can be estimated using the ratio between T1- and T2-weighted structural MRI. However, acquiring multiple imaging modalities is challenging in patients with inattentive disorders. In this study, we proposed a comprehensive framework to provide multiple imaging features related to the brain microstructure using only T1-weighted MRI. Our toolbox consists of (i) synthesizing T2-weighted MRI from T1-weighted MRI using a conditional generative adversarial network; (ii) estimating microstructural features, including intracortical covariance and moment features of cortical layer-wise microstructural profiles; and (iii) generating a microstructural gradient, which is a low-dimensional representation of the intracortical microstructure profile. We trained and tested our toolbox using T1- and T2-weighted MRI scans of 1,104 healthy young adults obtained from the Human Connectome Project database. We found that the synthesized T2-weighted MRI was very similar to the actual image and that the synthesized data successfully reproduced the microstructural features. The toolbox was validated using an independent dataset containing healthy controls and patients with episodic migraine as well as the atypical developmental condition of autism spectrum disorder. Our toolbox may provide a new paradigm for analyzing multimodal structural MRI in the neuroscience community and is openly accessible at https://github.com/CAMIN-neuro/GAN-MAT.

1. Introduction

Multimodal magnetic resonance imaging (MRI) enables the investigation of brain structure and function and their relationships *in vivo*. Using structural MRI of T1-weighted (T1w) and T2-weighted (T2w) images, we can assess the anatomical features of the brain, such as cortical thickness, curvature, and volume. Both T1w and T2w data elucidate brain structures, but the image contrast is a major difference. In T1w MRI, the white matter is bright, and the gray matter is dark, whereas T2w imaging shows the opposite intensity patterns. This is a consequence of the different MRI parameters. For example, in T1w, the repetition time (TR), which is the time between successive pulse sequences applied to the same slice, and the echo time (TE), which is the time from the center of the radio-frequency pulse to the center of the echo, were shorter than those in T2w MRI. A short TR leads to a strong T1 weighting, whereas a long TE results in a strong T2 weighting.

---

* Corresponding author at: Department of Data Science, Inha University, Incheon, South Korea.
E-mail address: boyong.park@inha.ac.kr (B.-y. Park).

https://doi.org/10.1016/j.neuroimage.2024.120595
Received 23 April 2023; Received in revised form 25 March 2024; Accepted 28 March 2024

Indeed, T1 and T2 properties are heterogeneous across different tissue types according to the amount of available free water, yielding different image contrasts (Stanisz et al., 2005).

In addition to brain morphology, we can assess microstructural information of the brain using T1w and T2w MRI without obtaining cytoarchitecture data. An approximation of the brain microstructure can be estimated using a microstructure-sensitive proxy, which is calculated based on the ratio between T1w and T2w imaging contrasts (Glasser et al., 2014; Glasser and van Essen, 2011), enabling us to investigate the cortical microstructure *in vivo*. A recent study suggested a method for analyzing the interregional relations of the brain microstructure (Paquola et al., 2019b) by calculating cortical layer-wise microstructural profiles among different brain regions. By applying dimensionality reduction techniques, they generated a low-dimensional representation of the cortical microstructure, referred to as a microstructural gradient. The microstructural gradient represents a well-known hierarchical cortical model of the sensory-fugal axis, which expands from the sensory regions to the limbic cortices (Mesulam, 1998; Paquola et al., 2019b). This feature has been widely adopted to assess the microstructural profiles of the brain in healthy adults as well as during adolescence (Paquola et al., 2019b; Whitaker et al., 2016). Indeed, the microstructural gradient linked the macroscale connectome to microscale cell-type-specific expression during adolescent development, suggesting the validity of this feature for investigating multiscale properties of the brain (Paquola et al., 2019a). However, obtaining microstructural features is challenging because it requires acquiring both T1w and T2w MRI, which is time-consuming and costly. Moreover, obtaining multiple imaging data within a restricted time may not be possible for individuals with psychiatric disorders showing inattentive behaviors, such as autism spectrum disorder and attention-deficit/hyperactivity disorder. Because of these issues, many open databases and clinics typically provide only T1w MRI, not T2w, for research (Di Martino et al., 2017, 2014; Milham et al., 2012; Nooner et al., 2012). One approach for mitigating this limitation is image synthesis. If we can synthesize T2w MRI images from T1w images, we can generate a microstructural gradient using only T1w MRI images with reduced time and cost.

Image synthesis has been conducted in many prior works using natural images and texts (Huang et al., 2018; Sangkloy et al., 2016; Thies et al., 2019; Wang et al., 2017; Zhang et al., 2017), and transferred to study medical imaging data (Chira et al., 2022; Nie et al., 2018; Osokin et al., 2017; Shin et al., 2018). For example, one study generated high-resolution images from low-resolution data using deep variational autoencoders (VAE) (Chira et al., 2022), and another work generated brain MRI with tumors using a generative adversarial network (GAN) (Huang et al., 2021; Osokin et al., 2017). Additionally, one study synthesized multiple imaging modalities using GAN, such as computed tomography from MRI, 7T MRI from 3T MRI, and T2w from T1w MRI (Nie et al., 2018). GAN is a deep learning model synthesizing new imaging data consisting of a generator and discriminator (Goodfellow et al., 2014). The GAN model generates data by adversarially training the generator and the discriminator. The generator makes fake images as similar as possible to the original image, and the discriminator distinguishes whether the input images are fake or real. Specifically, the generator is trained to make the discriminator fail to classify between fake and real data, and the discriminator is trained to distinguish between real and fake images as accurately as possible. A recent study introduced a conditional GAN by adding specific conditions to the vanilla GAN (Nie et al., 2018). One representative model of the conditional GAN is pix2pix, which processes paired data of input and label images (Isola et al., 2016), and another model, called CycleGAN, allows the unpaired set of images (Zhu et al., 2017).

Several studies have proposed models for synthesizing T2w MRI images from T1w MRI images (Kawahara and Nagata, 2021; Yang et al., 2020; Zhao et al., 2021). However, these studies are limited to yielding two-dimensional (2D) MRI data or focus on improving the accuracy of image synthesis without providing a comprehensive framework to study the brain microstructure *in vivo*. In this study, we propose a toolbox consolidating (i) the synthesis of T2w MRI images from T1w images using a 3D-based conditional GAN model, (ii) the calculation of a microstructure-sensitive proxy based on the T1w/T2w ratio, and (iii) the generation of ready-to-use microstructural features (Fig. 1A).

2. Methods

2.1. Imaging data

We studied structural MRI data from three independent sites: (i) Human Connectome Project (HCP) (http://www.humanconnectome.org/) (Van Essen et al., 2013), (ii) Samsung Medical Center (SMC), and (iii) Autism Brain Imaging Data Exchange II initiative (ABIDE-II; https://fcon_1000.projects.nitrc.org/indi/abide) (Di Martino et al., 2017). The GAN model was constructed using healthy young adults from the HCP dataset, and its generalizability was validated using the healthy and diseased populations from the SMC dataset. Finally, we applied the model to the ABIDE-II dataset to confirm its generalizability to both typical and atypical neurodevelopmental conditions. The detailed image acquisition parameters are as follows:

i) HCP: We obtained T1w and T2w data of 1104 healthy young adults (mean ± standard deviation (SD) age = 28.8 ± 3.7 years; 54.9 % female) from the HCP database. The T1w MRI was performed using a 3D magnetization-prepared rapid acquisition gradient echo (MPRAGE) sequence (TR = 2400 ms; TE = 2.14 ms; field of view (FOV) = 224 × 224 mm^2; voxel size = 0.7 mm isotropic; number of slices = 256), and the T2w MRI was performed using a 3D T2-SPACE sequence (TR = 3200 ms; TE = 565 ms; FOV = 224 × 224 mm^2, voxel size = 0.7 mm isotropic, number of slices = 256). The imaging and phenotypic data are publicly available and anonymized. The Washington University Institutional Review Board (IRB) previously approved the participant recruitment procedures and informed consent forms, including consent to share de-identified data, as part of the HCP.

ii) SMC: From the SMC site, we obtained T1w and T2w data of 43 healthy controls (mean ± SD age = 35.1 ± 7.6 years; 76.7 % female) and 58 individuals with migraine (mean ± SD age = 34.3 ± 8.2 years; 75.8 % female). The T1w MRI was scanned turbo field echo (TFE) sequence (TR = 8.2 ms; TE = 3.8 ms; field of view (FOV) = 256 × 256 mm^2; voxel size = 1.0 mm isotropic; and the number of slices = 180), and the T2w MRI was scanned turbo spin echo (TSE) sequence (TR = 3000 ms; TE = 280 ms; FOV = 256 × 256 mm^2, voxel size = 1.0 mm isotropic, and the number of slices = 180). The SMC IRB approved this study, and all participants provided written informed consent. This study is part of an ongoing longitudinal project registered at ClinicalTrials.gov (Identifier: NCT03487978).

iii) ABIDE-II: We obtained T1w data of 535 neurotypical controls (mean ± SD age = 14.8 ± 9.3 years; 31.0 % female) and 470 individuals with autism (mean ± SD age = 14.8 ± 9.2 years; 15.1 % female) from 17 different sites of the ABIDE-II database. As the database did not provide T2w MRI data, we only studied T1w data. The acquisition parameters of each site are available elsewhere (https://fcon_1000.projects.nitrc.org/indi/abide). The data collection was performed in accordance with the local IRB guidelines. Following the Health Insurance Portability and Accountability Act (HIPAA) guidelines and 1000 Functional Connectomes Project/INDI protocols, all ABIDE datasets were fully anonymized, with no protected health information included.

2.2. MRI data preprocessing

i) HCP: The HCP data were preprocessed using the minimal preprocessing pipelines for HCP (Glasser et al., 2013). The T1w and T2w data were corrected for gradient nonlinearity and b0 distortions and co-registered using a rigid-body transformation. Bias field correction was performed based on the inverse intensities from T1- and T2-weighting. The processed data were nonlinearly registered to the

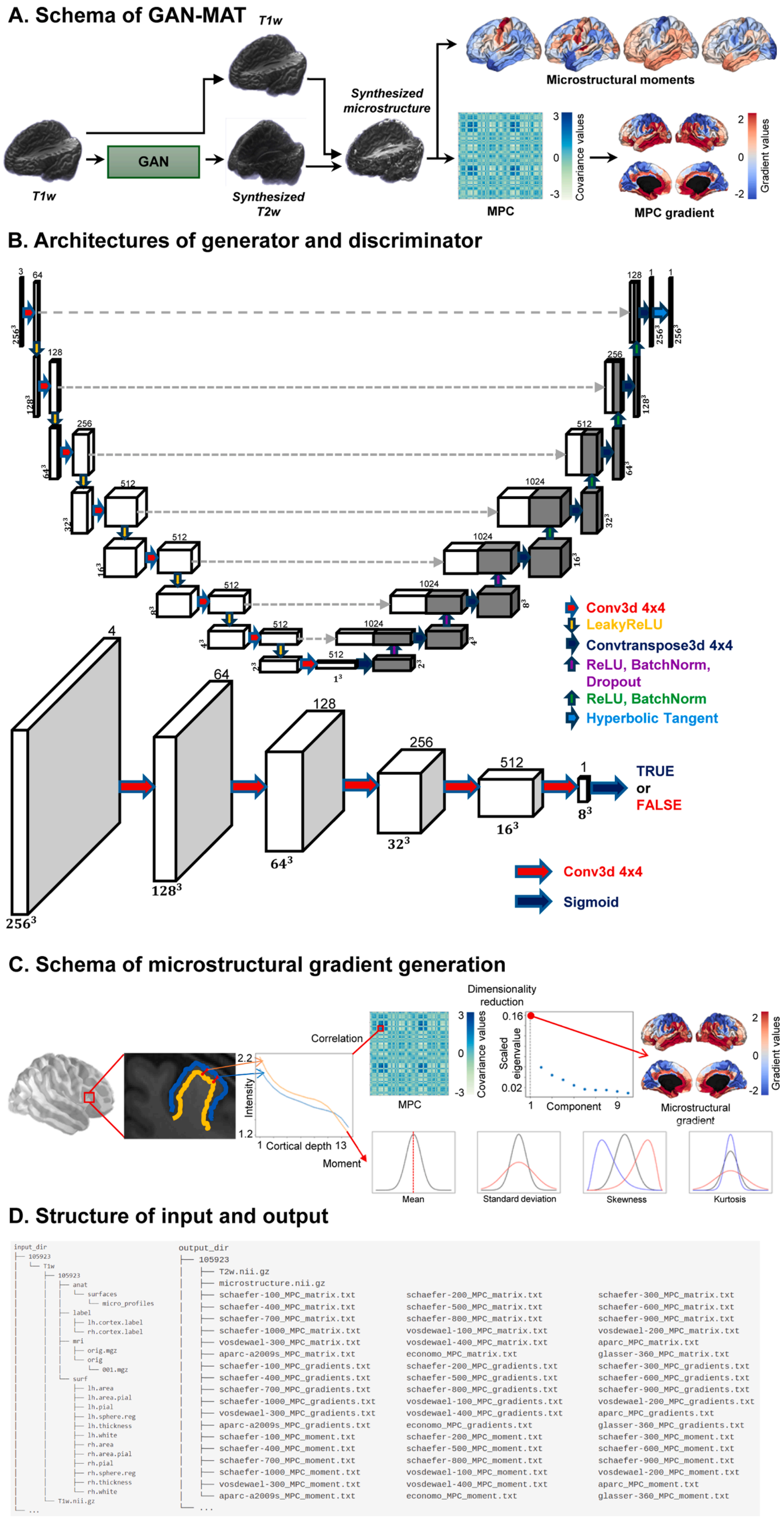

```
input_dir
├── 105923
│   └── T1w
│       ├── 105923
│       │   ├── anat
│       │   │   └── surfaces
│       │   │       └── micro_profiles
│       │   ├── label
│       │   │   ├── lh.cortex.label
│       │   │   └── rh.cortex.label
│       │   ├── mri
│       │   │   ├── orig.mgz
│       │   │   └── orig
│       │   │       └── 001.mgz
│       │   └── surf
│       │       ├── lh.area
│       │       ├── lh.area.pial
│       │       ├── lh.pial
│       │       ├── lh.sphere.reg
│       │       ├── lh.thickness
│       │       ├── lh.white
│       │       ├── rh.area
│       │       ├── rh.area.pial
│       │       ├── rh.pial
│       │       ├── rh.sphere.reg
│       │       ├── rh.thickness
│       │       └── rh.white
│       └── T1w.nii.gz
└── ...
```

```
output_dir
├── 105923
│   ├── T2w.nii.gz
│   ├── microstructure.nii.gz
│   ├── schaefer-100_MPC_matrix.txt       schaefer-200_MPC_matrix.txt       schaefer-300_MPC_matrix.txt
│   ├── schaefer-400_MPC_matrix.txt       schaefer-500_MPC_matrix.txt       schaefer-600_MPC_matrix.txt
│   ├── schaefer-700_MPC_matrix.txt       schaefer-800_MPC_matrix.txt       schaefer-900_MPC_matrix.txt
│   ├── schaefer-1000_MPC_matrix.txt      vosdewael-100_MPC_matrix.txt      vosdewael-200_MPC_matrix.txt
│   ├── vosdewael-300_MPC_matrix.txt      vosdewael-400_MPC_matrix.txt      aparc_MPC_matrix.txt
│   ├── aparc-a2009s_MPC_matrix.txt       economo_MPC_matrix.txt            glasser-360_MPC_matrix.txt
│   ├── schaefer-100_MPC_gradients.txt    schaefer-200_MPC_gradients.txt    schaefer-300_MPC_gradients.txt
│   ├── schaefer-400_MPC_gradients.txt    schaefer-500_MPC_gradients.txt    schaefer-600_MPC_gradients.txt
│   ├── schaefer-700_MPC_gradients.txt    schaefer-800_MPC_gradients.txt    schaefer-900_MPC_gradients.txt
│   ├── schaefer-1000_MPC_gradients.txt   vosdewael-100_MPC_gradients.txt   vosdewael-200_MPC_gradients.txt
│   ├── vosdewael-300_MPC_gradients.txt   vosdewael-400_MPC_gradients.txt   aparc_MPC_gradients.txt
│   ├── aparc-a2009s_MPC_gradients.txt    economo_MPC_gradients.txt         glasser-360_MPC_gradients.txt
│   ├── schaefer-100_MPC_moment.txt       schaefer-200_MPC_moment.txt       schaefer-300_MPC_moment.txt
│   ├── schaefer-400_MPC_moment.txt       schaefer-500_MPC_moment.txt       schaefer-600_MPC_moment.txt
│   ├── schaefer-700_MPC_moment.txt       schaefer-800_MPC_moment.txt       schaefer-900_MPC_moment.txt
│   ├── schaefer-1000_MPC_moment.txt      vosdewael-100_MPC_moment.txt      vosdewael-200_MPC_moment.txt
│   ├── vosdewael-300_MPC_moment.txt      vosdewael-400_MPC_moment.txt      aparc_MPC_moment.txt
│   └── aparc-a2009s_MPC_moment.txt       economo_MPC_moment.txt            glasser-360_MPC_moment.txt
└── ...
```

(caption on next page)

Fig. 1. A proposed toolbox synthesizing T2w MRI from T1w MRI and estimating brain microstructural features. (A) Shown is the schema of our toolbox, the Generative Adversarial Network-based Microstructural Profile Covariance Analysis Toolbox (GAN-MAT). It contains a conditional GAN synthesizing T2w from T1w MRI and calculates the ratio between T1w and T2w intensities to obtain the microstructure-sensitive proxy. The moment features are calculated from the synthesized microstructure data. The microstructural profile covariance (MPC) matrix is constructed based on the linear correlations of intracortical T1w/T2w intensity profiles between different brain regions, and microstructural gradients are generated using nonlinear dimensionality reduction techniques. **(B)** The architectures of the generator (top) and discriminator (bottom) are shown. **(C)** The schema for generating the microstructural gradient is shown. After generating 14 equivolumetric surfaces (left), we calculate linear correlations of cortical depth-dependent T1w/T2w intensity profiles between different cortical regions to make an MPC matrix (top middle). By applying dimensionality reduction techniques, we generate the microstructural gradient (top right). Additionally, four different moment features are calculated from the intracortical microstructural profiles (bottom right). **(D)** Shown is the organization of the input (left) and output (right) directories of a sample subject. *Abbreviations*: T1w, T1-weighted; T2w, T2-weighted; GAN, generative adversarial network; MRI, magnetic resonance imaging.

standard Montreal Neurological Institute (MNI152) space. White and pial surfaces were generated by following the boundaries between the different tissues (Dale et al., 1999; Fischl et al., 1999a, b). The mid-thickness surface was generated by averaging the white and pial surfaces and was used to generate the inflated surface. The spherical surface was registered to the Conte69 template using MSMAll (Glasser et al., 2016).

ii) SMC: The SMC data were preprocessed using the Fusion of Neuroimaging Preprocessing (FuNP) pipeline (Park et al., 2019) that integrated AFNI, FSL, FreeSurfer, and ANTs (Avants et al., 2011; Cox, 1996; Fischl, 2012; Glasser et al., 2013; Jenkinson et al., 2012). Similar to the HCP pipeline, gradient nonlinearity and b0 distortion correction, non-brain tissue removal, and intensity normalization were performed. White matter, pial, and mid-thickness surfaces were generated, and the inflated surface was spherically registered to the Conte69 template with 164k vertices and down-sampled to a 32k vertex mesh.

iii) ABIDE-II: T1w data from the ABIDE-II database were preprocessed using FreeSurfer (Dale et al., 1999; Fischl, 2012; Fischl et al., 2001; Fischl et al. 1999a, b; Ségonne et al., 2007), which included gradient non-uniformity correction, non-brain tissue removal, intensity normalization, and tissue segmentation. White and pial surfaces were generated, and topology correction, inflation, and spherical registration to the fsaverage template were performed.

2.3. T2w image synthesis using T1w MRI

Using the HCP data, we constructed a conditional GAN-based model to synthesize T2w images from T1w images. The participants were randomly divided into training ($n = 752$), validation ($n = 187$), and test ($n = 165$) datasets. The original 3D T1w data were registered onto a 0.8 mm isotropic MNI152 standard space with a matrix size of 227 × 272 × 227 using GNU parallel (Tange, 2018). After the tissue segmentation into gray matter, white matter, and cerebrospinal fluid using FAST (Zhang et al., 2001), normalization was applied to each tissue type and combined across the channels. The images were resized to 256 × 256 × 256 using cropping and zero-padding. The conditional GAN was based on the pix2pix, which was developed for 2D data (Isola et al., 2016). We adjusted the architecture to process the 3D T1w data (Fig. 1B). The generator was based on the U-Net architecture, which has skip connections linking the layers between the encoder and decoder (Isola et al., 2016). The data were processed using seven 3D convolutional layers with a leaky rectified linear unit (LeakyReLU) activation function. At the end of the encoding phase, the latent feature was convoluted, and 512 units were obtained. Three deconvolutions with ReLU, batch normalization, and dropout with a ratio of 0.5 were applied, and four additional deconvolutions with ReLU and batch normalization were conducted. Finally, deconvolution and a hyperbolic tangent were applied, and 256 × 256 × 256 output data were generated. The skip connection was linked to the corresponding decoding layer at each encoding layer. The discriminator was constructed using PatchGAN (Isola et al., 2016). It discriminates images in units of patches; thus, it is faster than conventional discriminators that distinguish entire images simultaneously. The 256 × 256 × 256 input matrix was passed through five convolution layers, and finally, a sigmoid function was applied. To optimize the hyperparameters, we adopted the Adam optimizer, which is a stochastic gradient descent method. The objective function was defined as follows:

$$\begin{aligned} arg\min_{G}\max_{D}\mathbb{E}_{x,\ y}[\log D(x,\ y)] + \ \mathbb{E}_{x}[\log(1 - D(x,\ G(x)))] \\ +100\ \times\ \mathbb{E}_{x,\ y}[\| \ y - G(x)\|_{1}] \end{aligned} \tag{1}$$

where G and D denote the generator and discriminator, and x and y denote the input and label images, respectively. The objective function comprises three terms: the first determines whether a label image is fake or real. The second term is an adversarial term in which the discriminator receives a fake image generated from the generator. The generator is trained to create fake images to enable the discriminator to classify the fake image as real, and the discriminator is trained to accurately distinguish between fake and real images. The last term is the regularization term for training stability. We assessed the performance of the model by calculating the mean absolute error (MAE), peak signal-to-noise ratio (PSNR), and structural similarity index measure (SSIM) between the actual and synthesized T2w data after normalizing the image intensities between zero and one. In addition to the global performance, we assessed the tissue type-specific synthesis performance of gray matter, white matter, and cerebrospinal fluid. Regional performance was assessed in the frontal, temporal, parietal, occipital, insular, and limbic cortices, and subcortical structures defined using the Brainnetome atlas (Fan et al., 2016). To evaluate the validity of the model hyperparameters, we assessed the synthesis performance by changing specific hyperparameters: (i) depth of the model = 6, 7, and 8; (ii) learning rate = 2e-04 and 1e-05; and (iii) number of kernels = 16, 32, and 64.

2.4. Microstructural profile of the brain

We generated a microstructure-sensitive proxy based on the ratio between the actual T1w and synthesized T2w contrasts (Glasser et al., 2014; Glasser and van Essen, 2011) (Fig. 1C). To calculate the intracortical microstructure profiles, we first generated 14 equivolumetric surfaces within the cortex between the inner white and outer pial surfaces and then sampled the T1w/T2w intensities along these surfaces (Paquola et al., 2019b). The statistical moment features (mean, SD, skewness, and kurtosis) were calculated from the intensity profiles (Paquola et al., 2019a; Schleicher et al., 2009). The mean and SD indicate the overall distribution of the intracortical microstructure, skewness represents shifts in intensity values toward the supragranular layers (*i.e.*, positive) or flat distribution (*i.e.*, negative), and kurtosis indicates whether the tails of the intensity distribution contain extreme values. In addition to the moment features, we constructed a microstructural profile covariance (MPC) matrix by calculating the linear correlations of cortical depth-dependent T1w/T2w intensity profiles between different cortical regions defined using the Schaefer atlas with 300 parcels (Schaefer et al., 2018), while controlling for the average whole-cortex intensity profile (Paquola et al., 2019b). The matrix was thresholded at zero and log-transformed (Coifman and Lafon, 2006). We generated a microstructural gradient from the MPC matrix, which is a low-dimensional representation of connectome organization that explains the spatial variation in connectivity (Margulies et al., 2016; Paquola et al., 2019b) using the BrainSpace toolbox (https://github.com/MICA-MNI/BrainSpace) (Vos de Wael et al., 2020). Specifically, we applied diffusion map embedding after applying a normalized angle kernel to the group-averaged MPC matrix, leaving the top 10 % of elements for each brain region (von Luxburg, 2007). Diffusion map embedding is a nonlinear dimensionality reduction technique that is robust to noise and computationally efficient compared with other nonlinear manifold learning techniques (Tenenbaum et al., 1995; von Luxburg, 2007). It is controlled by two parameters, α, and t, where α controls the influence of the density of the sampling points on the manifold ($\alpha = 0$, maximal influence; $\alpha = 1$, no influence), and t scales the eigenvalues of the diffusion operator. The parameters were set as $\alpha = 0.5$ and $t = 0$ to retain the global relations between data points in the embedded space following prior applications (Hong et al., 2019; Margulies et al., 2016; Paquola et al., 2019b; Park et al., 2021; Vos de Wael et al., 2020). Individual gradients were estimated and aligned to the template gradient using Procrustes alignment (Langs et al., 2015; Vos de Wael et al., 2020). We evaluated the similarity between the actual and synthesized microstructural moments and gradient features based on linear correlations, where the significance of the correlation was assessed using 1000 spin permutation tests that accounted for spatial autocorrelation (Alexander-Bloch et al., 2018; Vos de Wael et al., 2020).

2.5. *Generalizability of the model using an independent dataset*

To assess the reliability and robustness of our toolbox, we applied the HCP-driven model to an independent SMC dataset containing healthy controls and individuals with migraine. We synthesized T2w from T1w and calculated the microstructure-sensitive proxy and relevant moment and gradient features. Performance was evaluated using the MAE, PSNR, and SSIM between the actual and synthesized T2w images and the linear correlations between the actual and synthesized microstructural features.

2.6. *Age prediction and sex classification*

We validated the similarity of the actual and synthesized microstructural features by conducting (i) age prediction and (ii) sex classification using the actual or synthesized microstructural gradients. After randomly dividing the subjects into the training and test datasets, we used the least absolute shrinkage and selection operator regression framework for age prediction, and logistic regression for classifying male and female subjects. Additionally, we assessed the validity of the synthesized T2w images by performing a sex classification task using image descriptors, referred to as the keypoints (https://github.com/3dsift-rank) (Chauvin et al., 2022, 2020). In brief, the keypoints of the T2w image of each subject were extracted using the 3D scale-invariant feature transform (SIFT)-rank algorithm (Chauvin et al., 2020), and the keypoints were matched using the k-nearest neighbor. After calculating the pairwise image distances, sex classification was performed.

2.7. *Application to the developmental conditions*

We applied the toolbox to T1w MRI of neurotypical controls and individuals with autism obtained from the ABIDE-II database (Di Martino et al., 2017) to synthesize T2w data. As the ABIDE-II database did not provide T2w MRI data, we stratified the synthesized microstructural gradient values according to four cortical hierarchical levels (idiotypic, unimodal association, heteromodal association, and paralimbic) (Mesulam, 1998) to assess whether the gradient followed a well-known sensory-fugal brain hierarchy (Paquola et al., 2019b). Additionally, we assessed between-group differences in the synthesized microstructural gradient values between the neurotypical controls and individuals with autism. The two-sample *t*-tests were conducted, and multiple comparisons across the brain regions were corrected using $\mathrm{FDR} < 0.05$.

2.8. *Sensitivity analyses*

i) Bootstrap analysis. We trained the GAN model using different training and validation datasets and synthesized T2w MRI images from the T1w data. We assessed the performance of the model by calculating the MAE, PSNR, and SSIM between the actual and synthesized T2w images, as well as the microstructure-sensitive proxy (T1w/T2w ratio) of the test dataset. The analysis was repeated ten times.

ii) Two-dimensional model. Instead of the modified 3D pix2pix model, we evaluated the synthesis performance using the original 2D-based model. To this end, we sliced the 3D T1w images along each axis (x, y, and z). The original model consisted of one discriminator; however, we used three discriminators to distinguish the sliced images along each axis. Three synthesized images from the x-, y-, and z-axes were merged in the final stage to yield the 3D data. Model performance was assessed using the MAE, PSNR, and SSIM between the actual and synthesized T2w.

iii) Synthesis of T1w/T2w ratio. In addition to synthesizing T2w MRI images from T1w, we trained the GAN to synthesize T1w/T2w directly. We tested both the 2D and 3D models and calculated the MAE, PSNR, and SSIM to assess the performance.

iv) Evaluation using other models. In addition to the proposed model, we tested the synthesis performance using other deep learning models, such as VAE (Kingma and Welling, 2013), CycleGAN (Zhu et al., 2017), and latent diffusion model (LDM) (Rombach et al., 2021). The VAE is structured upon the autoencoder architecture. Unlike the vanilla autoencoder, VAE encodes input data as distributions instead of points, and the latent space has constraints such that the distributions returned by the encoder follow Gaussian distributions. Subsequently, the decoder generates output data similar to the input based on these distributions. Both the encoder and decoder consist of four convolution layers (with kernel size = 4, stride = 2, and zero-padding = 1), batch normalization, and ReLU activation function. The MAE is employed as the loss function, and the dimensions of the latent space are set to 256. The CycleGAN performs image-to-image translation tasks without requiring paired training data. It comprises two generators and two discriminators. The generators learn the mapping between two image domains to capture the target domain's characteristics. The first discriminator distinguishes real images from generated images in the target domain, and the second discriminator discerns real from generated images in the source domain. Each generator consists of three convolution encoder layers, nine residual blocks, and three deconvolution decoder layers. The encoder and decoder are composed of four convolution layers (kernel size = 4, stride = 2, and zero-padding = 1), instance normalization, and ReLU activation function. Each residual block comprises a double convolution layer (kernel size = 3, stride = 1, and zero-padding = 1) and a dropout layer with a rate of 0.5. The architecture of each discriminator is the same as our model. The adversarial loss in each domain and cycle consistency loss with a weight of 10 is used. The LDM is a probabilistic model that generates images starting with random noise and gradually transforms them into realistic images through a diffusion process. Unlike standard diffusion models, the LDM applies the diffusion process to latent features rather than raw pixel values. The encoder is constructed as follows: one convolution layer, three downsample processes (consisting of two residual blocks and one convolution layer), residual block, attention layer, residual block, and convolution layer. The decoder is the inverse of the encoder. The diffusion processing model comprises three encoder layers (attention layer, residual block, and downsample layer) and three decoder layers (attention layer, residual block, and upsample layer). While training, the encoder and decoder employ perceptual loss, adversarial loss, and Kullback-Leibler regularization in the latent space. MSE is used as the loss function to train the diffusion processing model.

3. Results

3.1. *Organization of the toolbox*

The developed toolbox requires the input data to be organized in a specific format containing T1w data and several FreeSurfer output files

(Fig. 1D). The toolbox can be implemented using a single command *"gan-mat -input_dir /INPUT/DATA/DIRECTORY -output_dir /OUTPUT/DIRECTORY"*. It then yields brain microstructural and intracortical moment features as well as the MPC matrix and its microstructural gradient, mapped onto 18 different parcellation schemes (Cruces et al., 2022).

3.2. Synthesis of T2w from T1w MRI

We synthesized 3D T2w MRI images from T1w data using a modified pix2pix model. The hyperparameters were set to the model depth of eight, the learning rate 2e-04, and the number of kernels 64 (**Supplementary Table 1**). The trained model was applied to the holdout test dataset, and the actual and synthesized T2w images showed similar spatial patterns (mean ± SD MAE of the whole brain across individuals = 0.012 ± 0.001; PSNR = 28.32 ± 0.573; SSIM = 0.941 ± 0.004) when the image intensity of each subject was scaled between zero and one (Fig. 2A and **Supplementary Table 2**). The synthesis performance was slightly different among the tissue types, with the best performance observed in the white matter (white matter = 0.036 ± 0.005, gray matter = 0.068 ± 0.005, and cerebrospinal fluid = 0.197 ± 0.013 across individuals). We stratified the MAE, PSNR, and SSIM according to different lobes and subcortical structures. The subcortical structures showed the best performance for MAE and PSNR, and the insular cortex showed the highest performance for SSIM. On the other hand, the lowest performance was observed in the parietal lobe for MAE, temporal lobe for PSNR, and frontal lobe for SSIM. However, the differences between different lobes and subcortical structures were trivial (Fig. 2A).

3.3. Synthesized brain microstructure

The validity of the synthesized T2w images was evaluated by assessing the similarity between the actual and synthesized microstructure-sensitive proxies based on the T1w/T2w ratio (Fig. 2B). We observed a high similarity in the synthesized microstructure-sensitive proxy, where the mean ± SD MAE was 0.005 ± 0.001, PSNR was 24.23 ± 0.685, and SSIM was 0.937 ± 0.003 across individuals (**Supplementary Table 2**). Moreover, the generated microstructural gradient showed a well-known sensory-fugal hierarchy that radiated from sensory and motor areas with higher myelination toward heteromodal associations and paralimbic regions with lower myelin content. The group-level correlations between the actual and synthesized microstructural gradients showed significant associations ($r = 0.96$, $p_{spin} < 0.001$; Fig. 2B). Additionally, the individual-level correlations were comparable (mean ± SD correlation coefficient across individuals = 0.87 ± 0.02, $p_{spin} < 0.001$). The similarity between the actual and synthesized moment features also showed high similarities (mean: $r = 0.98$, $p_{spin} < 0.001$; SD: $r = 0.94$, $p_{spin} < 0.001$; skewness: $r = 0.96$, $p_{spin} < 0.001$; kurtosis: $r = 0.93$, $p_{spin} < 0.001$; Fig. 2C).

3.4. Validation of the model using an independent dataset

The generalizability of the model was evaluated by applying it to an independent SMC dataset. The similarity between the actual and synthesized T2w images showed good results (mean ± SD MAE/PSNR/SSIM across healthy controls = 0.021 ± 0.001 / 23.55 ± 0.489 / 0.895 ± 0.005; individuals with migraine = 0.022 ± 0.002 / 23.54 ± 0.546 / 0.895 ± 0.008; Fig. 3A and **Supplementary Table 3–4**). The linear correlations were significant between the group-level actual and synthesized microstructural gradients (healthy controls: $r = 0.96$, $p_{spin} < 0.001$, individuals with migraine: $r = 0.97$, $p_{spin} < 0.001$; Fig. 3B) and moment features (healthy controls/individuals with migraine: mean = 0.57/0.52, SD = 0.77/0.79, skewness = 0.92/0.95, kurtosis = 0.87/0.90; Fig. 3C-D). These results indicated that our toolbox can be used to investigate the microstructural profiles of both healthy controls and patients with neurological conditions.

3.5. Age prediction and sex classification

Using the actual or synthesized microstructural gradients, we performed age prediction and sex classification tasks. We found that the performance of the age prediction was similar when we used actual or synthesized microstructural gradients ($r = 0.47$, $p = 0.001$ for actual gradient; $r = 0.46$, $p = 0.001$ for synthesized gradient; **Supplementary Fig. 1A**). The sex classification results were also comparable (accuracy = 77.8 % for both actual and synthesized gradients; **Supplementary Fig. 1B**). In addition, sex classification performance using keypoints (Chauvin et al., 2022) were comparable between the actual (accuracy = 78.8 %) and synthesized T2w images (73.2 %), indicating that our synthesized T2w images may preserve the biological properties of the actual data.

3.6. Application of the model to typical and atypical developmental conditions

We applied our toolbox to data from neurotypical controls and individuals with autism, which we obtained from the ABIDE II database (Di Martino et al., 2017). We estimated the MPC matrix and microstructural gradients for each subject and averaged them to obtain group-representative data for the control and autism groups (Fig. 4A). The generated microstructural gradients exhibited a sensory-fugal axis in both groups. When we stratified the gradient values according to the four cortical hierarchical levels (Mesulam, 1998), a hierarchy along the cortex was observed, expanding from the lower-level idiotypic to the higher-order association and paralimbic areas (Fig. 4B). When we assessed between-group differences in the synthesized microstructural gradients between the control and autism groups, we found significant (FDR < 0.05) between-group differences in the microstructural gradient values in the superior temporal cortex and precuneus (**Supplementary Fig. 2**), which were consistent with previous studies (Carper et al., 2017). Together, these results indicate that our toolbox can be generalized to independent datasets of typical and atypical developmental conditions.

3.7. Sensitivity analyses

i) Bootstrap analysis. We synthesized T2w data from T1w MRI images using randomly selected training and validation datasets to avoid subject-selection bias. The mean ± SD MAE/PSNR/SSIM between the actual and synthesized T2w of the test datasets across ten bootstraps was 0.012 ± 0.0001 / 28.20 ± 0.183 / 0.921 ± 0.004 (**Supplementary Fig. 3**), and that of the T1w/T2w ratio was 0.005 ± 0.0001 / 24.25 ± 0.126 / 0.936 ± 0.0007, indicating robustness.

ii) Two-dimensional model. The 2D-based model was trained instead of the modified 3D model. The mean ± SD MAE/PNSR/SSIM between the actual and synthesized T2w was 0.020 ± 0.002 / 25.03 ± 0.614 / 0.844 ± 0.004 (**Supplementary Fig. 4A** and **Supplementary Table 2**). We quantitatively compared the performance between the 2D and 3D models by conducting a paired *t*-test using the MAE/PSNR/SSIM between the two models. We found significant differences between the 2D and 3D models (MAE: $t = -251$, $p < 0.001$; PSNR: $t = 291$, $p < 0.001$; SSIM: $t = 646$, $p < 0.001$), indicating that the 3D method performs better than the 2D method in synthesizing T2w.

iii) Synthesis of T1w/T2w ratio. Instead of synthesizing T2w, we directly generated the T1w/T2w ratio from the T1w data. The 2D model showed mean ± SD MAE/PSNR/SSIM of 0.008 ± 0.001 / 24.24 ± 0.570 / 0.901 ± 0.020 (**Supplementary Fig. 4A** and **Supplementary Table 2**), and the 3D model showed 0.006 ± 0.001 / 24.98 ± 0.511 / 0.928 ± 0.003 (**Supplementary Fig. 4A** and **Supplementary Table 2**). When we compared the performance between the 2D and 3D models, we found significant differences ($t = -18.8$ and $p < 0.001$), indicating that the 3D method performs better than the 2D method not only for synthesizing T2w but also T1w/T2w ratio. Additionally, we compared the

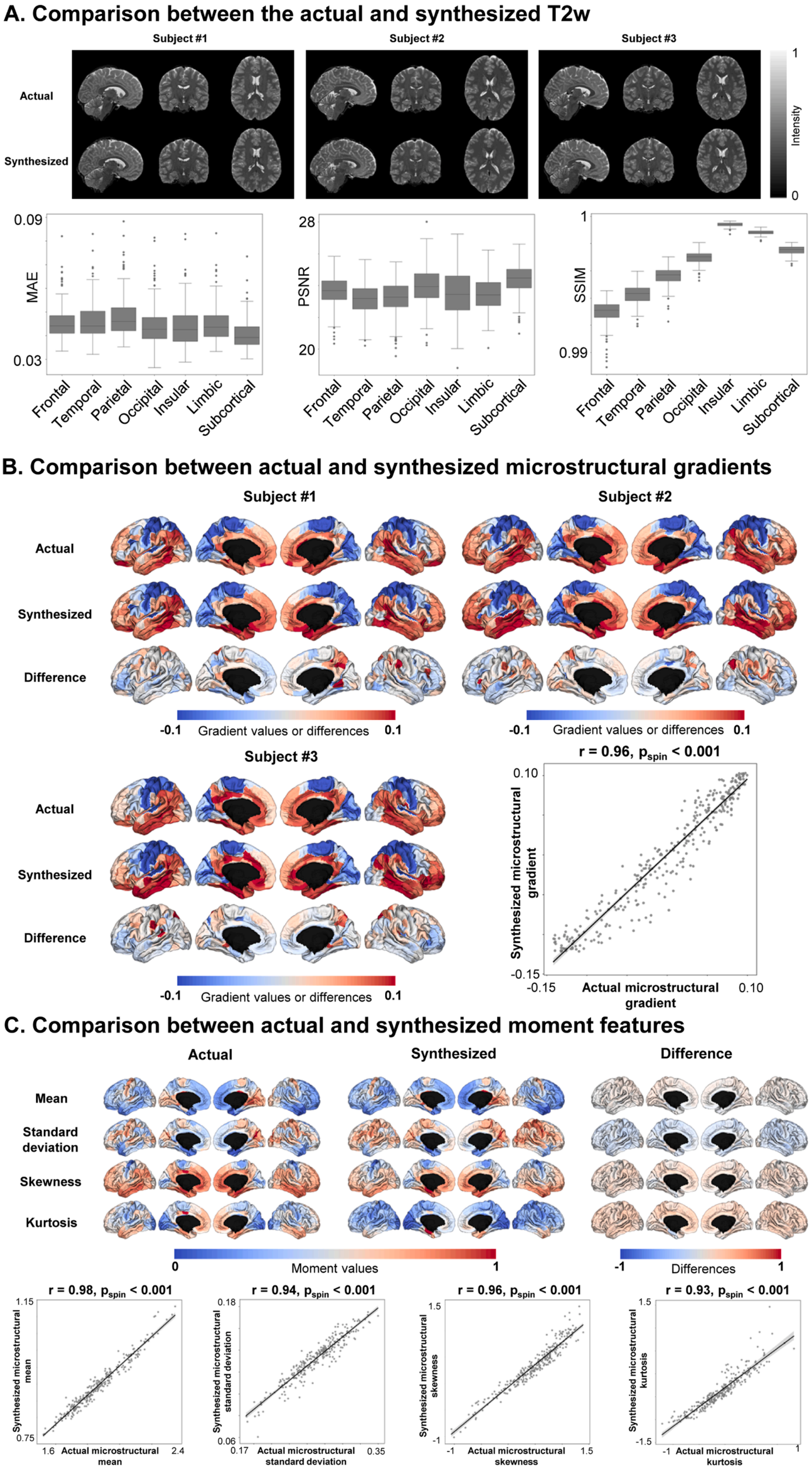

(caption on next page)

Fig. 2. Performance of the synthesis model. (A) Visualization of the actual and synthesized T2w images of three representative participants (top). The box plots show the MAE, PSNR, and SSIM of different cortical and subcortical structures (bottom). **(B)** The actual and synthesized microstructural gradients and their differences of the three representative participants. The similarity of the group-level gradients is assessed using spatial correlations with spin permutation tests (bottom right), where the gray area indicates a 95 % confidence interval. **(C)** The actual and synthesized group-level moment features and their differences are shown. The scatter plots indicate group-level correlations between actual and synthesized moment features (bottom). *Abbreviations:* T2w, T2-weighted; MAE, mean absolute error; PNSR, peak signal-to-noise ratio; SSIM, structural similarity index measure.

performance of calculating the T1w/T2w ratio after synthesizing the T2w image and the method directly synthesizing the T1w/T2w ratio. We conducted a paired *t*-test of the correlation coefficients between the actual and synthesized microstructural gradients derived from two different methods. We found significant differences ($t = 49.02$ and $p < 0.001$) between the two approaches, indicating that calculating the T1w/T2w ratio using the synthesized T2w data is better than synthesizing the T1w/T2w ratio directly.

iv) Evaluation using other models. We tested the performance of synthesizing T2w images from T1w data using other types of deep learning models. We found that our 3D-based model (mean ± SD MAE of the whole brain across individuals = 0.012 ± 0.001; PSNR = 28.32 ± 0.573; SSIM = 0.941 ± 0.004) outperformed VAE (MAE = 0.023 ± 0.005; PSNR = 24.45 ± 1.056; SSIM = 0.757 ± 0.039), CycleGAN (MAE = 0.024 ± 0.003; PSNR = 23.85 ± 0.772; SSIM = 0.771 ± 0.014), and LDM (MAE = 0.032 ± 0.003; PSNR = 25.95 ± 0.484; SSIM = 0.518 ± 0.053; **Supplementary Table 2**). Our model also showed good performance in synthesizing T1w/T2w ratio (**Supplementary Table 2**). When we evaluated the performance of the models applied to the independent SMC dataset, our model also showed the best results (**Supplementary Table 3–4**).

4. Discussion

The image synthesis approach benefits neuroimaging studies by generating multiple imaging modalities from a single modal image with reduced time and cost. In this study, we constructed and disseminated a toolbox to analyze the brain microstructure *in vivo* using only T1w MRI. Specifically, the toolbox synthesizes T2w from T1w MRI and calculates a microstructure-sensitive proxy to generate the MPC matrix, its gradient, and moment features. We observed a high correspondence between the actual and synthesized features, and multiple sensitivity analyses demonstrated the robustness of the toolbox. Our proposed framework may facilitate multimodal neuroimaging studies, particularly for studying brain microstructures using limited neuroimaging modalities.

The concept of image synthesis was introduced in previous neuroimaging studies. For example, one study used a conditional GAN to synthesize T1w from T2w images and T2w from T1w images based on the original pix2pix model (Kawahara and Nagata, 2021). Another study modified the model to process 3D data, in which each dimension was a sagittal, coronal, or axial slice (Zhao et al., 2021). Additionally, a conditional GAN was adopted to improve the quality of the registration and segmentation of brain images containing tumors (Yang et al., 2020). These studies focused on optimizing the distribution of the synthesized image to make it as similar as possible to an actual image. Thus, the aims of these studies were primarily to improve the synthesis accuracy and optimize the hyperparameters of the model. Contrastingly, our work aimed to provide the microstructural features of the brain that can be used in neuroscience and clinical studies to identify markers of specific psychiatric or neurological conditions. For example, the microstructure-sensitive proxy can be used to investigate alterations in brain network organization of Alzheimer’s disease, schizophrenia, epilepsy, and multiple sclerosis (Bernhardt et al., 2018; Boaventura et al., 2022; Ganzetti et al., 2015; Pelkmans et al., 2019; Yasuno et al., 2017), and we can assess behavioral and cognitive traits during typical and atypical development (Carper et al., 2017; Darki et al., 2021; Langensee et al., 2022). Moreover, microstructural features can be used to investigate multiscale neural organization. The microstructural gradient describes macroscopic connectome organization and is associated with gene expression in brain cells (Paquola et al., 2019a; Royer et al., 2020). Inl summary, our study impacts clinical neuroscience by providing a consolidated framework for synthesizing T2w images from T1w MRI images and generating ready-to-use brain microstructural features.

We demonstrated the reliability and robustness of our toolbox using multiple scenarios. First, we quantitatively tested four different models: (i) synthesis of T2w using a 3D GAN (ii) 2D GAN, (iii) synthesis of the T1w/T2w ratio using a 3D GAN, and (iv) 2D GAN. We found that the first model (3D–T2w synthesis) exhibited the best performance. The superior performance of the 3D model relative to that of the 2D model may be due to the quantity of information. The 2D model uses information on the brain anatomy of each axis (*i.e.*, sagittal, coronal, and axial) for training; thus, it does not consider the geometric properties across different slices. Additionally, we found that synthesizing T2w images is better than directly creating a T1w/T2w ratio. A previous study suggested that the role of T2w images when calculating microstructure-sensitive proxies is to remove blood vessels and dura from the pial surface and reduce the effects of myelin content on pial surface generation via intensity normalization of gray matter (Glasser et al., 2014). If we directly synthesize the T1w/T2w ratio from the T1w data, the GAN model may not consider these biological properties of T2w images, leading to a low similarity between the actual and synthesized images. Second, we tested the generalizability of our toolbox by using an independent dataset containing both healthy and diseased populations. These findings indicate that our toolbox is appropriate for investigating disease-related microstructural alterations in the brain using only T1w MRI. Lastly, we conducted age prediction and sex classification tasks using T2w images and microstructural gradient values. Our results support that the synthesized data using our model might preserve the biological properties of the actual data. The findings provided reliability of the synthesized microstructural features, again indicating the usefulness of our synthesis model.

There are several limitations in our study. First, the loss function we used was based on the L1 norm and binary cross-entropy, which is solely based on statistical properties rather than biological characteristics. Future works are required to develop loss or regularization functions that reflect the biological properties of the structural images. Second, U-Net architecture may be adjusted to enhance performance. Future works could consider a nested U-Net architecture (UNet++) that replaced skip-connection with a re-designed skip pathway, resulting in improved task performance (Zhou et al., 2018). Additionally, integrating the attention layers into the U-Net architecture could embed demographic information, such as sex or age, which may enhance the performance of each individual. Third, our sensitivity analysis revealed that our GAN-based model outperformed the vanilla LDM. This might be due to the insufficient training data. The diffusion-based models often require larger training data than GAN-based models. In future works, we will merge multiple datasets or consider diffusion-based models that work well on a small data size to improve the synthesis performance. Lastly, our toolbox currently supports synthesizing T2w from T1w but not the inverse. To perform multimodal tasks for T1w to T2w and T2w to T1w, other deep learning models could be considered.

In this study, we developed an end-to-end toolbox for synthesizing T2w images from T1w images and generating brain microstructural features, including MPC matrix, microstructural gradients, and moment features. The reliability and robustness of this toolbox were validated based on multiple sensitivity analyses, enabling the study of the brain

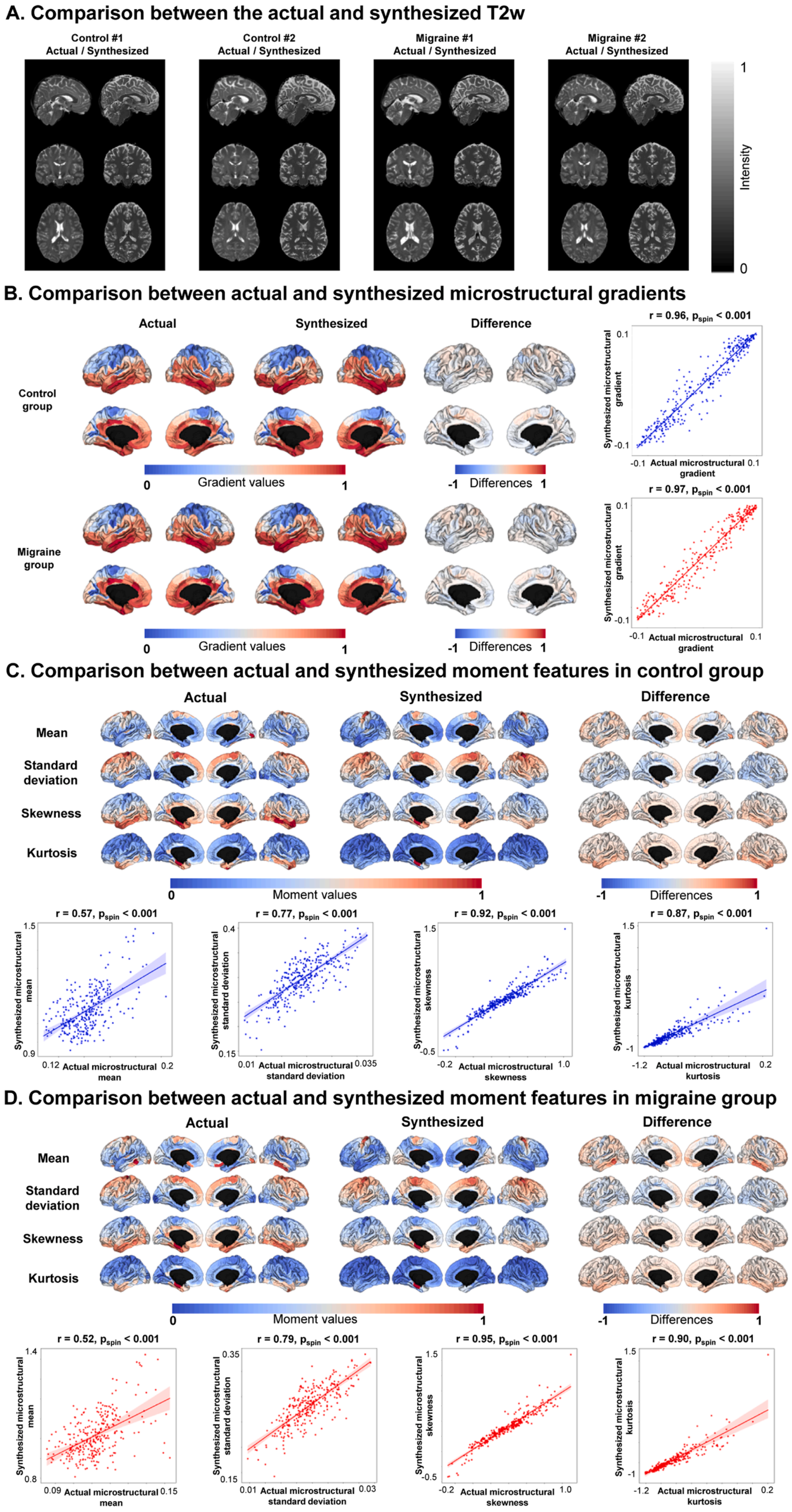

Fig. 3. Validation of the toolbox using an independent dataset. **(A)** Visualization of the actual and synthesized T2w images of two representative participants in each group. **(B)** Shown are the actual and synthesized microstructural gradients and their differences of the control and migraine groups, respectively. The group-level correlations between the actual and synthesized gradients are shown with scatter plots. **(C)** We described moment features of the control and **(D)** migraine groups, where the group-level correlations are reported with scatter plots. *Abbreviations:* T2w, T2-weighted.

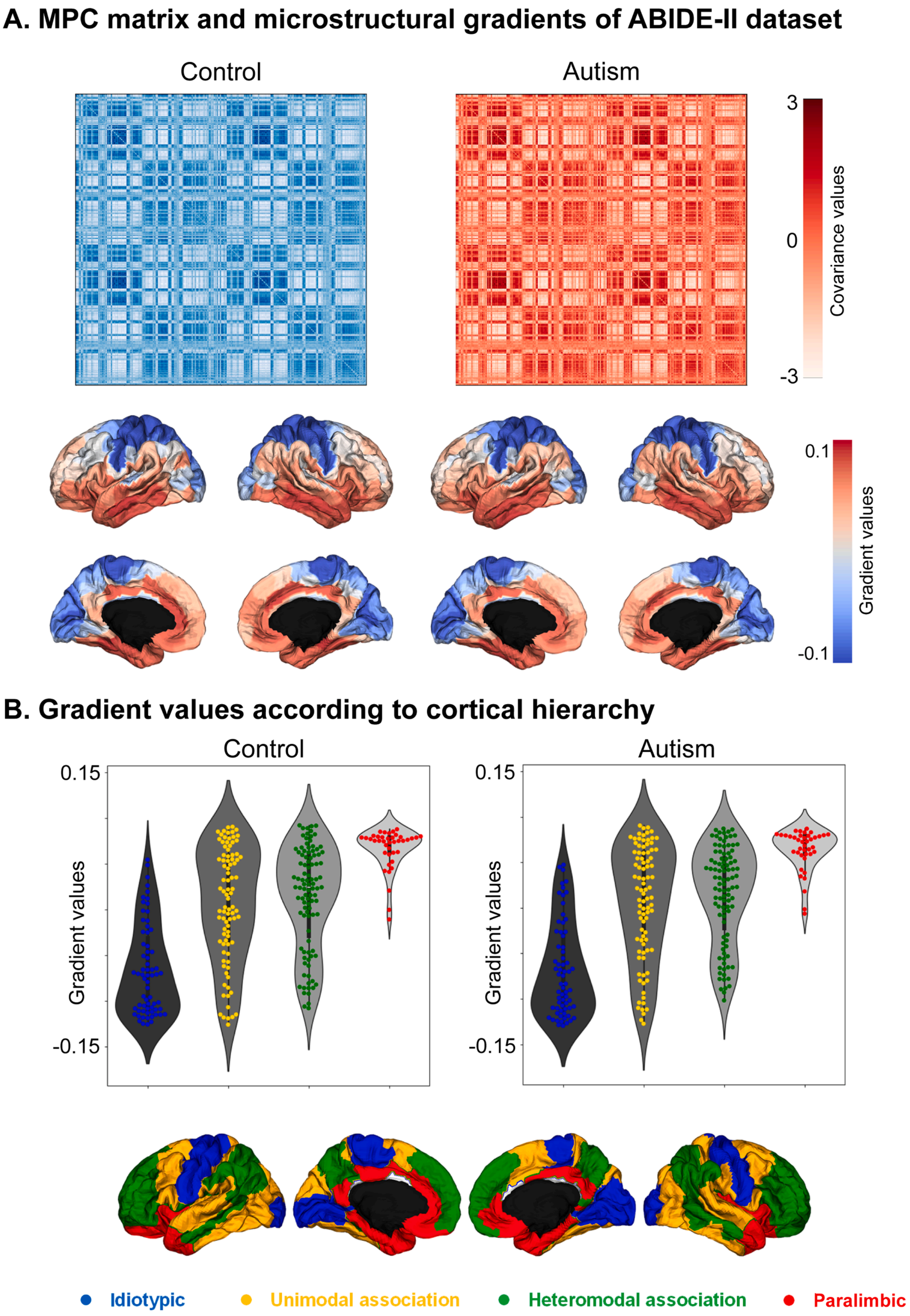

Fig. 4. Brain microstructure of an independent dataset. (A) We constructed a microstructural profile covariance (MPC) matrix (top) and microstructural gradient (bottom) of neurotypical controls and individuals with autism. **(B)** We stratified the gradient values according to four cortical hierarchical levels.

microstructure *in vivo* using only T1w MRI. Our toolbox may help researchers in the neuroscience community to foster future multimodal MRI studies to investigate brain microstructures.

Code availability

The codes for the GAN-MAT are available at https://github.com/CAMIN-neuro/GAN-MAT.

Funding

Dr. Bo-yong Park was funded by the National Research Foundation of Korea (NRF-2022R1A5A7033499), Institute for Information and Communications Technology Planning and Evaluation (IITP) funded by the Korea Government (MSIT) (No. 2022–0–00448, Deep Total Recall: Continual Learning for Human-Like Recall of Artificial Neural Networks; No. RS-2022–00155915, Artificial Intelligence Convergence Innovation Human Resources Development (Inha University)). Drs. Bo-yong Park and Hyunjin Park were jointly supported by the IITP funded by the Korea Government (MSIT) (No. 2021–0–02068, Artificial Intelligence Innovation Hub) and Institute for Basic Science (IBS-R015-D1). Dr. Mi Ji Lee was supported by the National Research Foundation of Korea (NRF-2020R1A2B5B01001826) and the New Faculty Startup Fund from Seoul National University. Drs. Casey Paquola and Boris C. Bernhardt were funded in part by Helmholtz Association's Initiative and Networking Fund under the Helmholtz International Lab grant agreement InterLabs-0015, and the Canada First Research Excellence Fund (CFREF Competition 2, 2015–2016) awarded to the Healthy Brains, Healthy Lives initiative at McGill University, through the Helmholtz International BigBrain Analytics and Learning Laboratory (HIBALL).

Data availability

The imaging and phenotypic data were provided, in part, by the Human Connectome Project, the WU-Minn Consortium (https://www.humanconnectome.org/), and the Autism Brain Imaging Data Exchange initiative (ABIDE-II; https://fcon_1000.projects.nitrc.org/indi/abide/). The SMC data are available on request from the corresponding author and are not publicly available due to Institutional Review Board restrictions.

CRediT authorship contribution statement

Yeongjun Park: Writing – original draft, Visualization, Validation, Software, Resources, Methodology, Formal analysis, Data curation, Conceptualization. **Mi Ji Lee:** Writing – review & editing, Funding acquisition, Data curation. **Seulki Yoo:** Writing – review & editing, Investigation. **Chae Yeon Kim:** Writing – review & editing, Methodology. **Jong Young Namgung:** Writing – review & editing, Methodology. **Yunseo Park:** Writing – review & editing, Methodology. **Hyunjin Park:** Writing – review & editing, Resources, Methodology. **Eun-Chong Lee:** Writing – review & editing, Methodology. **Yeo Dong Yoon:** Writing – review & editing. **Casey Paquola:** Writing – review & editing, Resources, Methodology, Investigation, Funding acquisition. **Boris C. Bernhardt:** Writing – review & editing, Resources, Methodology, Investigation, Funding acquisition. **Bo-yong Park:** Methodology, Investigation, Funding acquisition, Formal analysis, Data curation, Conceptualization, Project administration, Resources, Software, Supervision, Validation, Visualization, Writing – original draft.

Declaration of competing interest

Bo-yong Park is an Associate Editor for NeuroImage but was not involved in the handling or review process of this manuscript.

Supplementary materials

Supplementary material associated with this article can be found, in the online version, at doi:10.1016/j.neuroimage.2024.120595.

References

Alexander-Bloch, A.F., Shou, H., Liu, S., Satterthwaite, T.D., Glahn, D.C., Shinohara, R.T., Vandekar, S.N., Raznahan, A., 2018. On testing for spatial correspondence between maps of human brain structure and function. Neuroimage 178, 540–551. https://doi.org/10.1016/j.neuroimage.2018.05.070.

Avants, B.B., Tustison, N.J., Song, G., Cook, P.A., Klein, A., Gee, J.C., 2011. A reproducible evaluation of ANTs similarity metric performance in brain image registration. Neuroimage 54, 2033–2044. https://doi.org/10.1016/j.neuroimage.2010.09.025.

Bernhardt, B.C., Fadaie, F., Vos de Wael, R., Hong, S.J., Liu, M., Guiot, M.C., Rudko, D.A., Bernasconi, A., Bernasconi, N., 2018. Preferential susceptibility of limbic cortices to microstructural damage in temporal lobe epilepsy: A quantitative T1 mapping study. Neuroimage 182, 294–303. https://doi.org/10.1016/j.neuroimage.2017.06.002.

Boaventura, M., Sastre-Garriga, J., Garcia-Vidal, A., Vidal-Jordana, A., Quartana, D., Carvajal, R., Auger, C., Alberich, M., Tintoré, M., Rovira, À., Montalban, X., Pareto, D., 2022. T1/T2-weighted ratio in multiple sclerosis: A longitudinal study with clinical associations. Neuroimage Clin. 34 https://doi.org/10.1016/j.nicl.2022.102967.

Carper, R.A., Treiber, J.M., White, N.S., Kohli, J.S., Müller, R.A., 2017. Restriction spectrum imaging as a potential measure of cortical neurite density in autism. Front. Neurosci. 10 https://doi.org/10.3389/fnins.2016.00610.

Chauvin, L., Kumar, K., Desrosiers, C., Wells, W., Toews, M., 2022. Efficient Pairwise Neuroimage Analysis Using the Soft Jaccard Index and 3D Keypoint Sets. IEEe Trans. Med. ImAging 41, 836–845. https://doi.org/10.1109/TMI.2021.3123252.

Chauvin, L., Kumar, K., Wachinger, C., Vangel, M., de Guise, J., Desrosiers, C., Wells, W., Toews, M., 2020. Neuroimage signature from salient keypoints is highly specific to individuals and shared by close relatives. Neuroimage 204. https://doi.org/10.1016/j.neuroimage.2019.116208.

Chira, D., Haralampiev, I., Winther, O., Dittadi, A., Liévin, V., 2022. Image Super-Resolution With Deep Variational Autoencoders.

Coifman, R.R., Lafon, S., 2006. Diffusion maps. Appl. Comput. Harmon. Anal. 21, 5–30. https://doi.org/10.1016/j.acha.2006.04.006.

Cox, R.W., 1996. AFNI: Software for Analysis and Visualization of Functional Magnetic Resonance Neuroimages. Computers and Biomedical Research.

Cruces, R.R., Royer, J., Herholz, P., Larivière, S., Vos de Wael, R., Paquola, C., Benkarim, O., Park, B., yong, Degré-Pelletier, J., Nelson, M.C., DeKraker, J., Leppert, I.R., Tardif, C., Poline, J.B., Concha, L., Bernhardt, B.C., 2022. Micapipe: A pipeline for multimodal neuroimaging and connectome analysis. Neuroimage 263. https://doi.org/10.1016/j.neuroimage.2022.119612.

Dale, A.M., Fischl, B., Sereno, M.I., 1999. Cortical Surface-Based Analysis I. Segmentation and Surface Reconstruction.

Darki, F., Nyström, P., Mcalonan, G., Bölte, S., Falck-Ytter, T., 2021. T1-Weighted/T2-Weighted Ratio Mapping at 5 Months Captures Individual Differences in Behavioral Development and Differentiates Infants at Familial Risk for Autism from Controls. Cerebral Cortex 31, 4068–4077. https://doi.org/10.1093/cercor/bhab069.

Di Martino, A., O'Connor, D., Chen, B., Alaerts, K., Anderson, J.S., Assaf, M., Balsters, J. H., Baxter, L., Beggiato, A., Bernaerts, S., Blanken, L.M.E., Bookheimer, S.Y., Braden, B.B., Byrge, L., Castellanos, F.X., Dapretto, M., Delorme, R., Fair, D.A., Fishman, I., Fitzgerald, J., Gallagher, L., Keehn, R.J.J., Kennedy, D.P., Lainhart, J.E., Luna, B., Mostofsky, S.H., Müller, R.A., Nebel, M.B., Nigg, J.T., O'Hearn, K., Solomon, M., Toro, R., Vaidya, C.J., Wenderoth, N., White, T., Craddock, R.C., Lord, C., Leventhal, B., Milham, M.P., 2017. Enhancing studies of the connectome in autism using the autism brain imaging data exchange II. Sci Data 4. https://doi.org/10.1038/sdata.2017.10.

Di Martino, A., Yan, C.G., Li, Q., Denio, E., Castellanos, F.X., Alaerts, K., Anderson, J.S., Assaf, M., Bookheimer, S.Y., Dapretto, M., Deen, B., Delmonte, S., Dinstein, I., Ertl-Wagner, B., Fair, D.A., Gallagher, L., Kennedy, D.P., Keown, C.L., Keysers, C., Lainhart, J.E., Lord, C., Luna, B., Menon, V., Minshew, N.J., Monk, C.S., Mueller, S., Müller, R.A., Nebel, M.B., Nigg, J.T., O'Hearn, K., Pelphrey, K.A., Peltier, S.J., Rudie, J.D., Sunaert, S., Thioux, M., Tyszka, J.M., Uddin, L.Q., Verhoeven, J.S., Wenderoth, N., Wiggins, J.L., Mostofsky, S.H., Milham, M.P., 2014. The autism brain imaging data exchange: Towards a large-scale evaluation of the intrinsic brain architecture in autism. Mol. Psychiatry 19, 659–667. https://doi.org/10.1038/mp.2013.78.

Fan, L., Li, H., Zhuo, J., Zhang, Y., Wang, J., Chen, L., Yang, Z., Chu, C., Xie, S., Laird, A. R., Fox, P.T., Eickhoff, S.B., Yu, C., Jiang, T., 2016. The Human Brainnetome Atlas: A New Brain Atlas Based on Connectional Architecture. Cerebral Cortex 26, 3508–3526. https://doi.org/10.1093/cercor/bhw157.

Fischl, B., 2012. FreeSurfer. Neuroimage. https://doi.org/10.1016/j.neuroimage.2012.01.021.

Fischl, B., Liu, A., Dale, A.M., 2001. Automated Manifold Surgery: Constructing Geometrically Accurate and Topologically Correct Models of the Human Cerebral Cortex. IEEe Trans. Med. ImAging.

Fischl, B., Sereno, M.I., Dale, A.M., 1999a. Cortical Surface-Based Analysis II: Inflation. Flattening, and a Surface-Based Coordinate System.

Fischl, B., Sereno, M.I., Tootell, R.B.H., Dale, A.M., 1999b. High-Resolution Intersubject Averaging and a Coordinate System For the Cortical Surface, Hum. Brain Mapping.

Ganzetti, M., Wenderoth, N., Mantini, D., 2015. Mapping pathological changes in brain structure by combining T1- and T2-weighted MR imaging data. Neuroradiology. 57, 917–928. https://doi.org/10.1007/s00234-015-1550-4.

Glasser, M.F., Coalson, T.S., Robinson, E.C., Hacker, C.D., Harwell, J., Yacoub, E., Ugurbil, K., Andersson, J., Beckmann, C.F., Jenkinson, M., Smith, S.M., Van Essen, D. C., 2016. A multi-modal parcellation of human cerebral cortex. Nature 536, 171–178. https://doi.org/10.1038/nature18933.

Glasser, M.F., Goyal, M.S., Preuss, T.M., Raichle, M.E., Van Essen, D.C., 2014. Trends and properties of human cerebral cortex: Correlations with cortical myelin content. Neuroimage. https://doi.org/10.1016/j.neuroimage.2013.03.060.

Glasser, M.F., Sotiropoulos, S.N., Wilson, J.A., Coalson, T.S., Fischl, B., Andersson, J.L., Xu, J., Jbabdi, S., Webster, M., Polimeni, J.R., Van Essen, D.C., Jenkinson, M., 2013. The minimal preprocessing pipelines for the Human Connectome Project. Neuroimage 80, 105–124. https://doi.org/10.1016/j.neuroimage.2013.04.127.

Glasser, M.F., van Essen, D.C., 2011. Mapping human cortical areas in vivo based on myelin content as revealed by T1- and T2-weighted MRI. J. Neurosci. 31, 11597–11616. https://doi.org/10.1523/JNEUROSCI.2180-11.2011.

Goodfellow, I.J., Pouget-Abadie, J., Mirza, M., Xu, B., Warde-Farley, D., Ozair, S., Courville, A., Bengio, Y., 2014. Generative Adversarial Networks.

Hong, S.J., de Wael, R.V., Bethlehem, R.A.I., Lariviere, S., Paquola, C., Valk, S.L., Milham, M.P., Di Martino, A., Margulies, D.S., Smallwood, J., Bernhardt, B.C., 2019. Atypical functional connectome hierarchy in autism. Nat. Commun. 10 https://doi.org/10.1038/s41467-019-08944-1.

Huang, H., Yu, P.S., Wang, C., 2018. An Introduction to Image Synthesis with Generative Adversarial Nets.

Huang, P., Liu, X., Huang, Y., 2021. Data Augmentation For Medical MR Image Using Generative Adversarial Networks.

Isola, P., Zhu, J.Y., Zhou, T., Efros, A.A., 2016. Image-to-Image Translation with Conditional Adversarial Networks.

Jenkinson, M., Beckmann, C.F., Behrens, T.E.J., Woolrich, M.W., Smith, S.M., 2012. FSL. Neuroimage 62, 782–790. https://doi.org/10.1016/j.neuroimage.2011.09.015.

Kawahara, D., Nagata, Y., 2021. T1-weighted and T2-weighted MRI image synthesis with convolutional generative adversarial networks. Reports of Practical Oncology and Radiotherapy 26, 35–42. https://doi.org/10.5603/RPOR.a2021.0005.

Kingma, D.P., Welling, M., 2013. Auto-Encoding Variational Bayes.

Langensee, L., Rumetshofer, T., Behjat, H., Novén, M., Li, P., Mårtensson, J., 2022. T1w/T2w Ratio and Cognition in 9-to-11-Year-Old Children. Brain Sci. 12 https://doi.org/10.3390/brainsci12050599.

Langs, G., Golland, P., Ghosh, S.S., 2015. Predicting activation across individuals with resting-state functional connectivity based multi-atlas label fusion. Lecture Notes in Computer Science (Including Subseries Lecture Notes in Artificial Intelligence and Lecture Notes in Bioinformatics). Springer Verlag, pp. 313–320. https://doi.org/10.1007/978-3-319-24571-3_38.

Margulies, D.S., Ghosh, S.S., Goulas, A., Falkiewicz, M., Huntenburg, J.M., Langs, G., Bezgin, G., Eickhoff, S.B., Castellanos, F.X., Petrides, M., Jefferies, E., Smallwood, J., 2016. Situating the default-mode network along a principal gradient of macroscale cortical organization. Proc. Natl. Acad. Sci. u S. a 113, 12574–12579. https://doi.org/10.1073/pnas.1608282113.

Mesulam, M.M., 1998. From sensation to cognition. Brain.

Milham, P.M., Damien, F., Maarten, M., Stewart, H.M., 2012. The ADHD-200 Consortium: A model to advance the translational potential of neuroimaging in clinical neuroscience. Front. Syst. Neurosci. 1–5. https://doi.org/10.3389/fnsys.2012.00062.

Nie, D., Trullo, R., Lian, J., Wang, L., Petitjean, C., Ruan, S., Wang, Q., Shen, D., 2018. Medical Image Synthesis with Deep Convolutional Adversarial Networks. IEEE Trans. Biomed. Eng. 65, 2720–2730. https://doi.org/10.1109/TBME.2018.2814538.

Nooner, K.B., Colcombe, S.J., Tobe, R.H., Mennes, M., Benedict, M.M., Moreno, A.L., Panek, L.J., Brown, S., Zavitz, S.T., Li, Q., Sikka, S., Gutman, D., Bangaru, S., Schlachter, R.T., Kamiel, S.M., Anwar, A.R., Hinz, C.M., Kaplan, M.S., Rachlin, A.B., Adelsberg, S., Cheung, B., Khanuja, R., Yan, C., Craddock, C.C., Calhoun, V., Courtney, W., King, M., Wood, D., Cox, C.L., Kelly, A.M.C., Di Martino, A., Petkova, E., Reiss, P.T., Duan, N., Thomsen, D., Biswal, B., Coffey, B., Hoptman, M. J., Javitt, D.C., Pomara, N., Sidtis, J.J., Koplewicz, H.S., Castellanos, F.X., Leventhal, B.L., Milham, M.P., 2012. The NKI-Rockland sample: A model for accelerating the pace of discovery science in psychiatry. Front. Neurosci. https://doi.org/10.3389/fnins.2012.00152.

Osokin, A., Chessel, A., Salas, R.E.C., Vaggi, F., 2017. GANs for Biological Image Synthesis.

Paquola, C., Bethlehem, R.A., Seidlitz, J., Wagstyl, K., Romero-Garcia, R., Whitaker, K.J., Vos de Wael, R., Williams, G.B., Vértes, P.E., Margulies, D.S., Bernhardt, B., Bullmore, E.T., 2019a. Shifts in myeloarchitecture characterise adolescent development of cortical gradients. Elife 8. https://doi.org/10.7554/eLife.50482.

Paquola, C., Vos De Wael, R., Wagstyl, K., Bethlehem, R.A.I., Hong, S.J., Seidlitz, J., Bullmore, E.T., Evans, A.C., Misic, B., Margulies, D.S., Smallwood, J., Bernhardt, B. C., 2019b. Microstructural and functional gradients are increasingly dissociated in transmodal cortices. PLoS. Biol. 17 https://doi.org/10.1371/journal.pbio.3000284.

Park, B, yong, Hong, S.J., Valk, S.L., Paquola, C., Benkarim, O., Bethlehem, R.A.I., Di Martino, A., Milham, M.P., Gozzi, A., Yeo, B.T.T., Smallwood, J., Bernhardt, B.C., 2021. Differences in subcortico-cortical interactions identified from connectome and microcircuit models in autism. Nat. Commun. 12 https://doi.org/10.1038/s41467-021-21732-0.

Park, B.Y., Byeon, K., Park, H., 2019. FuNP (fusion of neuroimaging preprocessing) pipelines: A fully automated preprocessing software for functional magnetic resonance imaging. Front. Neuroinform. 13 https://doi.org/10.3389/fninf.2019.00005.

Pelkmans, W., Dicks, E., Barkhof, F., Vrenken, H., Scheltens, P., van der Flier, W.M., Tijms, B.M., 2019. Gray matter T1-w/T2-w ratios are higher in Alzheimer's disease. Hum. Brain Mapp. 40, 3900–3909. https://doi.org/10.1002/hbm.24638.

Rombach, R., Blattmann, A., Lorenz, D., Esser, P., Ommer, B., 2021. High-Resolution Image Synthesis with Latent Diffusion Models.

Royer, J., Paquola, C., Larivière, S., Vos de Wael, R., Tavakol, S., Lowe, A.J., Benkarim, O., Evans, A.C., Bzdok, D., Smallwood, J., Frauscher, B., Bernhardt, B.C., 2020. Myeloarchitecture gradients in the human insula: Histological underpinnings and association to intrinsic functional connectivity. Neuroimage 216. https://doi.org/10.1016/j.neuroimage.2020.116859.

Sangkloy, P., Lu, J., Fang, C., Yu, F., Hays, J., 2016. Scribbler: Controlling Deep Image Synthesis with Sketch and Color.

Schaefer, A., Kong, R., Gordon, E.M., Laumann, T.O., Zuo, X.N., Holmes, A.J., Eickhoff, S. B., Yeo, B.T.T., 2018. Local-Global Parcellation of the Human Cerebral Cortex from Intrinsic Functional Connectivity MRI. Cerebral Cortex 28, 3095–3114. https://doi.org/10.1093/cercor/bhx179.

Schleicher, A., Morosan, P., Amunts, K., Zilles, K., 2009. Quantitative architectural analysis: A new approach to cortical mapping. J. Autism. Dev. Disord. 39, 1568–1581. https://doi.org/10.1007/s10803-009-0790-8.

Ségonne, F., Pacheco, J., Fischl, B., 2007. Geometrically accurate topology-correction of cortical surfaces using nonseparating loops. IEEe Trans. Med. ImAging 26, 518–529. https://doi.org/10.1109/TMI.2006.887364.

Shin, H.C., Tenenholtz, N.A., Rogers, J.K., Schwarz, C.G., Senjem, M.L., Gunter, J.L., Andriole, K., Michalski, M., 2018. Medical Image Synthesis for Data Augmentation and Anonymization using Generative Adversarial Networks.

Stanisz, G.J., Odrobina, E.E., Pun, J., Escaravage, M., Graham, S.J., Bronskill, M.J., Henkelman, R.M., 2005. T1, T2 relaxation and magnetization transfer in tissue at 3T. Magn. Reson. Med. 54, 507–512. https://doi.org/10.1002/mrm.20605.

Tange, O., 2018. GNU Parallel 2018. https://doi.org/10.5281/zenodo.1146014.

Tenenbaum, J.B., de Silva, V., Langford, J.C., 1995. A Global Geometric Framework for Nonlinear Dimensionality Reduction. Philos. Trans. R. Soc. London Ser. B.

Thies, J., Zollhöfer, M., Nießner, M., 2019. Deferred neural rendering: Image Synthesis using Neural Textures. ACM Trans Graph 38. https://doi.org/10.1145/3306346.3323035.

Van Essen, D.C., Smith, S.M., Barch, D.M., Behrens, T.E.J., Yacoub, E., Ugurbil, K., 2013. The WU-Minn Human Connectome Project: An overview. Neuroimage 80, 62–79. https://doi.org/10.1016/j.neuroimage.2013.05.041.

von Luxburg, U., 2007. A Tutorial on Spectral Clustering.

Vos de Wael, R., Benkarim, O., Paquola, C., Lariviere, S., Royer, J., Tavakol, S., Xu, T., Hong, S.J., Langs, G., Valk, S., Misic, B., Milham, M., Margulies, D., Smallwood, J., Bernhardt, B.C., 2020. BrainSpace: a toolbox for the analysis of macroscale gradients in neuroimaging and connectomics datasets. Commun. Biol. 3 https://doi.org/10.1038/s42003-020-0794-7.

Wang, T.C., Liu, M.Y., Zhu, J.Y., Tao, A., Kautz, J., Catanzaro, B., 2017. High-Resolution Image Synthesis and Semantic Manipulation with Conditional GANs.

Whitaker, K.J., Vértes, P.E., Romero-Garciaa, R., Váša, F., Moutoussis, M., Prabhu, G., Weiskopf, N., Callaghan, M.F., Wagstyl, K., Rittman, T., Tait, R., Ooi, C., Suckling, J., Inkster, B., Fonagy, P., Dolan, R.J., Jones, P.B., Goodyer, I.M., Bullmore, E.T., 2016. Adolescence is associated with genomically patterned consolidation of the hubs of the human brain connectome. Proc. Natl. Acad. Sci. u S. a 113, 9105–9110. https://doi.org/10.1073/pnas.1601745113.

Yang, Q., Li, N., Zhao, Z., Fan, X., Chang, E.I.C., Xu, Y., 2020. MRI Cross-Modality Image-to-Image Translation. Sci. Rep. 10 https://doi.org/10.1038/s41598-020-60520-6.

Yasuno, F., Kazui, H., Morita, N., Kajimoto, K., Ihara, M., Taguchi, A., Yamamoto, A., Matsuoka, K., Takahashi, M., Nakagawara, J., Iida, H., Kishimoto, T., Nagatsuka, K., 2017. Use of T1-weighted/T2-weighted magnetic resonance ratio to elucidate changes due to amyloid β accumulation in cognitively normal subjects. Neuroimage Clin. 13, 209–214. https://doi.org/10.1016/j.nicl.2016.11.029.

Zhang, H., Xu, T., Li, H., Zhang, S., Wang, X., Huang, X., Metaxas, D., 2017. StackGAN++: Realistic Image Synthesis with Stacked Generative Adversarial Networks.

Zhang, Y., Brady, M., Smith, S., 2001. Segmentation of Brain MR Images Through a Hidden Markov Random Field Model and the Expectation-Maximization Algorithm. IEEe Trans. Med. ImAging.

Zhao, P., Pan, H., Xia, S., 2021. MRI-Trans-GAN: 3D MRI Cross-Modality Translation. In: Chinese Control Conference, CCC. IEEE Computer Society, pp. 7229–7234. https://doi.org/10.23919/CCC52363.2021.9550256.

Zhou, Z., Siddiquee, M.M.R., Tajbakhsh, N., Liang, J., 2018. UNet++: A Nested U-Net Architecture for Medical Image Segmentation.

Zhu, J.Y., Park, T., Isola, P., Efros, A.A., 2017. Unpaired Image-to-Image Translation using Cycle-Consistent Adversarial Networks.